Monthly Notices
of the
ROYAL ASTRONOMICAL SOCIETY
MNRAS **456,** 1791–1802 (2016) doi:10.1093/mnras/stv2771

Orbital and superorbital variability of LS I +61 303 at low radio frequencies with GMRT and LOFAR

B. Marcote,[1⋆] M. Ribó,[1⋆†] J. M. Paredes,[1⋆] C. H. Ishwara-Chandra,[2] J. D. Swinbank,[3] J. W. Broderick,[4,5] S. Markoff,[6] R. Fender,[4] R. A. M. J. Wijers,[6] G. G. Pooley,[7] A. J. Stewart,[4] M. E. Bell,[8,9] R. P. Breton,[10,5] D. Carbone,[6] S. Corbel,[11,12] J. Eislöffel,[13] H. Falcke,[14,15] J.-M. Grie smeier,[16,12] M. Kuniyoshi,[17] M. Pietka,[18] A. Rowlinson,[6,15] M. Serylak,[12,19,20] A. J. van der Horst,[21] J. van Leeuwen,[6,15] M. W. Wise[6,15] and P. Zarka[12,22]

Affiliations are listed at the end of the paper

Accepted 2015 November 22. Received 2015 November 16; in original form 2015 July 31

ABSTRACT

LS I +61 303 is a gamma-ray binary that exhibits an outburst at GHz frequencies each orbital cycle of ≈26.5 d and a superorbital modulation with a period of ≈4.6 yr. We have performed a detailed study of the low-frequency radio emission of LS I +61 303 by analysing all the archival Giant Metrewave Radio Telescope data at 150, 235 and 610 MHz, and conducting regular LOw Frequency ARray observations within the Radio Sky Monitor (RSM) at 150 MHz. We have detected the source for the first time at 150 MHz, which is also the first detection of a gamma-ray binary at such a low frequency. We have obtained the light curves of the source at 150, 235 and 610 MHz, all of them showing orbital modulation. The light curves at 235 and 610 MHz also show the existence of superorbital variability. A comparison with contemporaneous 15-GHz data shows remarkable differences with these light curves. At 15 GHz we see clear outbursts, whereas at low frequencies we see variability with wide maxima. The light curve at 235 MHz seems to be anticorrelated with the one at 610 MHz, implying a shift of ∼0.5 orbital phases in the maxima. We model the shifts between the maxima at different frequencies as due to the expansion of a one-zone emitting region assuming either free–free absorption or synchrotron self-absorption with two different magnetic field dependences. We always obtain a subrelativistic expansion velocity, in some cases being close to the stellar wind one.

Key words: radiation mechanisms: non-thermal – binaries: close – stars: individual: LS I +61 303 – gamma-rays: stars – radio continuum: stars.

1 INTRODUCTION

Binary systems comprising a young massive star and a compact object can exhibit non-thermal emission from radio to gamma rays. A fraction of these systems displays a spectral energy distribution dominated by the MeV-GeV photons, thus becoming classified as gamma-ray binaries (see Dubus 2013 for a review). Only five gamma-ray binary systems are known at present: PSR B1259−63 (Aharonian et al. 2005b), LS 5039 (Aharonian et al. 2005a), LS I +61 303 (Albert et al. 2006), HESS J0632+057 (Hinton et al. 2009; Skilton et al. 2009), and 1FGL J1018.6−5856 (Fermi LAT Collaboration et al. 2012). PSR B1259−63 is the only system which is confirmed to host a pulsar; the natures of the compact objects are currently unknown for the remaining sources.

The multiwavelength emission from these sources can be explained by synchrotron and inverse Compton (IC) emission, within the context of various models. Although the particle acceleration mechanisms remain unclear, two different scenarios have been proposed. On the one hand, the microquasar scenario posits the existence of an accretion disc, corona and relativistic jets in the system, with the particle acceleration driven by accretion/ejection processes (Mirabel 2006). On the other hand, the young non-accreting pulsar scenario establishes the existence of a shock between the relativistic wind of the pulsar and the non-relativistic wind of the companion star, where particles can be accelerated up to relativistic energies (Dubus 2013).

⋆E-mail: bmarcote@am.ub.es (BM); mribo@am.ub.es (MR); jmparedes@ub.edu (JMP)
† Serra Húnter Fellow.

The gamma-ray binary LS I +61 303 (also known as V615 Cas) is a system composed of a young main-sequence B0 Ve star and a compact object orbiting it with a period $P_{\rm orb} = 26.4960 \pm 0.0028$ d (Gregory 2002) and an eccentricity $e = 0.72 \pm 0.15$ (Casares et al. 2005). The system is located at 2.0 ± 0.2 kpc according to H I measurements (Frail & Hjellming 1991), with coordinates $\alpha_{\rm J2000} = 2^{\rm h}40^{\rm m}31\overset{\rm s}{.}7$ and $\delta_{\rm J2000} = +61^\circ13'45\overset{''}{.}6$ (Moldón 2012). Assuming the epoch of the first radio observation as the origin of the orbital phase, $\rm JD_0 = 2443\,366.775$, the periastron passage takes place in the orbital phase range 0.23–0.28 (Casares et al. 2005; Aragona et al. 2009). LS I +61 303 was initially identified as the counterpart of a gamma-ray source detected by *COS B* (Hermsen et al. 1977), and subsequently an X-ray counterpart was also detected (Bignami et al. 1981). X-ray observations with *RXTE*/ASM revealed an orbital X-ray modulation (Paredes et al. 1997). The system was also coincident with an EGRET source above 100 MeV (Kniffen et al. 1997) and finally it was detected as a TeV emitter by MAGIC (Albert et al. 2006), which was later confirmed by VERITAS (Acciari et al. 2008). An orbital modulation of the TeV emission was also found by MAGIC (Albert et al. 2009). A correlation between the TeV and X-ray emission was revealed using MAGIC and X-ray observations, which together with the observed X-ray/TeV flux ratio, supports leptonic models with synchrotron X-ray emission and IC TeV emission (Anderhub et al. 2009; but see Acciari et al. 2009). Finally, *Fermi*/LAT reported GeV emission, orbitally modulated and anticorrelated with respect to the X-ray/TeV emission (Abdo et al. 2009).

The 1–10 GHz radio light curve of LS I +61 303 is also orbitally modulated, showing a clear outburst each orbital cycle that increases the $\lesssim 50$ mJy steady flux density emission up to ∼100–200 mJy. These outbursts are periodic, although changes in their shape and intensity have been reported from cycle to cycle (Paredes, Estalella & Rius 1990; Ray et al. 1997). Strickman et al. (1998) studied the evolution of a single outburst with multifrequency observations in the range 0.33–23 GHz. The outburst is detected at all frequencies, but the flux density peaks first at the highest frequencies, and later at the lower ones. A low-frequency turnover was also suggested to be present in the range 0.3–1.4 GHz (Strickman et al. 1998).

A long-term modulation is also observed at all wavelengths in LS I +61 303, the so-called superorbital modulation, with a period $P_{\rm so} = 1\,667 \pm 8$ d or ∼4.6 yr (Gregory 2002). This modulation was first found at GHz radio frequencies (Paredes 1987; Gregory et al. 1989; Paredes et al. 1990), affecting the amplitude of the non-thermal outbursts and the orbital phases at which the onset and peak of these outbursts take place, drifting from orbital phases of ∼0.45 to ∼0.95 (Gregory 2002). The source exhibits the minimum activity at GHz frequencies during the superorbital phase range of $\phi_{\rm so} \sim 0.2$–0.5, whereas the maximum activity takes place at $\phi_{\rm so} \sim 0.78$–0.05, assuming the same $\rm JD_0$ as for the orbital phase. A similar behaviour is also observed in optical photometric and Hα equivalent width observations that trace the thermal emission of the source (Paredes-Fortuny et al. 2015). The origin of the superorbital modulation could be related to periodic changes in the circumstellar disc and the mass-loss rate of the Be star (Zamanov et al. 2013), although other interpretations within the framework of a precessing jet are still discussed (see Massi & Torricelli-Ciamponi 2014, and references therein).

At milliarcsecond scales LS I +61 303 has been observed and resolved several times (Massi et al. 2001, 2004; Dhawan, Mioduszewski & Rupen 2006; Albert et al. 2008; Moldón 2012). Dhawan et al. (2006) showed a changing morphology as a function of the orbital phase, resembling a cometary tail. Albert et al. (2008) observed similar morphological structures at similar orbital phases to those considered in Dhawan et al. (2006). Later on, Moldón (2012) also reported this behaviour: the morphology of LS I +61 303 changes periodically within the orbital phase. These morphological changes have been interpreted as evidence of the pulsar scenario (Dubus 2006, 2013), although other interpretations have also been suggested (see Massi, Ros & Zimmermann 2012, and references therein). It must be noted that radio pulsation searches have also been conducted with unsuccessful results (McSwain et al. 2011; Cañellas et al. 2012).

At the lowest frequencies ($\lesssim 1$ GHz), only a few observations have been published up to now. Pandey et al. (2007) conducted two observations of LS I +61 303 at 235 and 610 MHz simultaneously with the Giant Metrewave Radio Telescope (GMRT; Ananthakrishnan 1995). They observed a positive spectral index of $\alpha \approx 1.3$ (defined as $S_\nu \propto \nu^\alpha$, where S_ν is the flux density at a frequency ν) in both epochs and reported variability at both frequencies at a 2.5σ and 20σ level, respectively. Although Strickman et al. (1998) also observed the source at 330 MHz three times during one outburst, given the large uncertainties of the measured flux densities they could not infer variability at more than the 1σ level. At these low frequencies we should observe the presence of different absorption mechanisms, such as synchrotron self-absorption (SSA), free–free absorption (FFA) or the Razin effect, as found for other gamma-ray binaries (see e.g. Marcote et al. 2015 for the case of LS 5039). In addition, at these low frequencies we should also expect extended emission at about arcsec scales originating from the synchrotron emission from low-energy particles (Bosch-Ramon 2009; Durant et al. 2011).

In this paper, we present the first deep and detailed study of the radio emission from LS I +61 303 at low frequencies through GMRT and LOw Frequency ARray (LOFAR; van Haarlem et al. 2013) data to unveil its behaviour along the orbit. We compare the results with contemporaneous high-frequency observations conducted with the Ryle Telescope (RT) and the Owens Valley Radio Observatory (OVRO) 40-m telescope. In Section 2, we present all the radio data analysed in this work together with the data reduction and analysis processes. In Section 3, we present the obtained results and in Section 4 we discuss the observed behaviour of LS I +61 303 in the context of the known orbital and superorbital variability. Our conclusions are presented in Section 5.

2 OBSERVATIONS AND DATA REDUCTION

To reveal the orbital behaviour of LS I +61 303 at low radio frequencies, we have analysed data from different instruments and different epochs. These data include archival GMRT observations from a monitoring programme in 2005–2006, as well as three additional archival observations from 2005 and 2008. They also include a LOFAR commissioning observation in 2011 and five LOFAR observations performed in 2013. RT and OVRO observations at 15 GHz, contemporaneous to these low-frequency observations, have also been analysed to obtain a complete picture of the behaviour of the source. In Fig. 1, we summarize all these observations in a frequency versus time diagram. The first seven columns of Table 1 shows the log of the low-frequency observations.

2.1 Archival GMRT observations

The GMRT monitoring covers the observations performed between 2005 November 24 and 2006 February 7, at 235 and 610 MHz, simultaneously. These data sets include 25 observations spread over

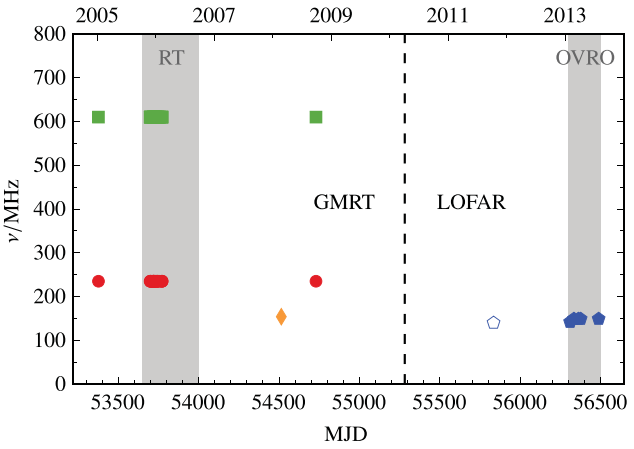

Figure 1. Summary of all the data presented in this work in a frequency versus time diagram (Modified Julian Date, MJD, on the bottom axis and calendar year on the top axis). The vertical dashed line separates the GMRT data (left) from the LOFAR data (right). Green squares represent the 610-MHz GMRT observations, red circles correspond to the simultaneous GMRT observations at 235 MHz, the orange diamond shows the 154-MHz GMRT data and the blue pentagons represent the LOFAR observations at ≈150 MHz. The open pentagon corresponds to the commissioning LOFAR observation, which is not considered in the results of this work. The grey bands indicate the time intervals during which 15-GHz RT and OVRO observations used in this work were conducted.

this time interval, all of them obtained with a single IF, with single circular polarization at 235 MHz (LL) and 610 MHz (RR). The 235 and 610 MHz data have bandwidths of 8 and 16 MHz, divided into 64 and 128 channels, respectively. These observations display a wide range of observing times, from 30 min to 11 h (see column 7 in Table 1). 3C 48, 3C 147 and 3C 286 were used as amplitude calibrators, and 3C 119 (0432+416) or 3C 48 as phase calibrators.

In addition to the previous monitoring, there are also three isolated archival GMRT observations. Two of these observations were carried out on 2005 January 7 and on 2008 September 20, at 235 and 610 MHz, using the same setup as that described above. The remaining observation was performed at 154 MHz on 2008 February 18, with dual circular polarization (LL and RR) and a bandwidth of 16 MHz divided into 128 channels. 3C 48, 3C 147 and 3C 286 were again used as amplitude calibrators, and 3C 119 was the phase calibrator for the three observations.

The GMRT data were calibrated and analysed using standard procedures within AIPS,[1] although OBIT[2] (Cotton 2008), PARSELTONGUE[3] (Kettenis et al. 2006) and SPAM[4] (Intema et al. 2009) have also been used to develop scripts that call AIPS tasks to easily reduce the whole data set.

We loaded and flagged the raw visibilities in AIPS, removing telescope off-source times, instrumental problems or radio frequency interference (RFI). A first calibration using a unique channel, free of RFI, was performed on the data, and after that we bandpass calibrated them. A more accurate flagging process was performed later on and we finally calibrated the full data set in amplitude and phase, taking into account the previous bandpass calibration. The target source was imaged and self-calibrated several times to correct for phase and amplitude errors that were not properly corrected during the previous calibration, using a Briggs robust weighting of zero in the cleaning process (Briggs 1995). As the GMRT field of view at these low frequencies covers a few degrees (between ∼5 and 1°.5 at 154 and 610 MHz, respectively), we needed to consider the full *uvw*-space during the imaging process (Thompson 1999) and correct the final images for the primary beam attenuation. The GMRT observation performed on 2005 November 28 could not be properly calibrated and hence could not provide results, leading to a total of 24 flux density measurements. In the observations performed on 2005 December 30, 2006 January 19 and 21, the 235 MHz data could not be properly calibrated: the runs were relatively short and a large amount of data had to be flagged, thus providing clean images that were not good enough to self-calibrate the data, preventing the collection of reliable flux densities.

After this data reduction process, we also performed a correction of the system temperature, $T_{\rm sys}$, for each antenna to subtract the contribution of the Galactic diffuse emission, relevant at low frequencies (see a detailed explanation in the appendix of Marcote et al. 2015). The obtained $T_{\rm sys}$ corrections were directly applied to the flux densities of the final target images. We note that these corrections imply an additional source of uncertainty that does not affect the relative flux density variations from one epoch to another at a given frequency. The uncertainties introduced in the flux densities are close to the typical root-mean-square (rms) values obtained at 235 and 610 MHz, but at 154 MHz the uncertainties increased from ≈5 per cent to ≈20 per cent.

The measurement of the flux densities in each image was done using the `tvstat` and `jmfit` tasks of AIPS, both of them providing consistent values in all cases. We determined the rms noise of the images using `tvstat` in a region around the source without including it nor any background source.

To guarantee the reliability of the measured flux densities, we monitored the flux density values of four background sources detected in the field of view of LS I +61 303. The lack of a similar trend in all sources allows us to be confident that the variability described below is intrinsically related to LS I +61 303 and not due to calibration issues.

2.2 LOFAR observations

We have also analysed several LOFAR observations conducted with the High Band Antennas. First, we conducted a deep 6-h LOFAR observation at 140 MHz during its commissioning stage on 2011 September 30 to test the system and estimate the expected behaviour of LS I +61 303 at these low frequencies. This observation was performed using 23 core stations plus 9 remote stations, with a total bandwidth of 48 MHz divided in 244 subbands. These data show a large rms noise level, with possible large uncertainties in the absolute flux density scale related to the calibration process. Hence we will not use these in this work (see preliminary results of this observation in Marcote et al. 2012).

In 2013, we conducted five 3-h LOFAR observations at around 150 MHz within the Radio Sky Monitor (RSM), which observes regularly several variable or transient radio sources (Fender et al. 2007). The target source was always centred on transit, using 23 core stations plus 13 remote stations. In four of these observations, we observed the source at 149 MHz with a total bandwidth of ≈0.8 MHz divided into four subbands. 3C 48 or 3C 147 were used as amplitude calibrators, observed in runs of 2 min interleaved in 11-min on-source runs. The observation on 2013 January 17 was

[1] The NRAO Astronomical Image Processing System, AIPS, is maintained by the National Radio Astronomy Observatory (NRAO). http://www.aips.nrao.edu.
[2] http://www.cv.nrao.edu/∼bcotton/Obit.html
[3] http://www.jive.nl/jivewiki/doku.php?id=parseltongue:parseltongue
[4] https://safe.nrao.edu/wiki/bin/view/Main/HuibIntemaSpam

Table 1. Summary of the low-frequency data presented in this work. Each row corresponds to one observation for which we show the facility used, the project code of the observation, the date (in calendar date and MJD) of the centre of the observation, the corresponding orbital phase $\phi_{\rm orb}$ (using $P_{\rm orb} = 26.4960$ d and $\rm JD_0 = 2443\,366.775$), the corresponding superorbital phase (assuming $P_{\rm so} = 1\,667$ d and the same $\rm JD_0$), the total time on source (t), and the flux densities at each frequency with the 1σ uncertainty (3σ upper limits in case of non-detections).

Facility	Project code	Date	MJD	$\phi_{\rm orb}$	$\phi_{\rm so}$	t (min)	$S_{\approx 150\,\rm MHz}$ (mJy)	$S_{235\,\rm MHz}$ (mJy)	$S_{610\,\rm MHz}$ (mJy)
GMRT	07PDA01[a]	2005-01-07	53377.47	0.84	0.01	30	–	34 ± 10	169 ± 3
GMRT	09PDA01	2005-11-24	53698.63	0.96	0.20	82	–	<31	89.9 ± 1.3
GMRT	09PDA01	2005-11-25	53699.71	0.00	0.20	56	–	<30	90 ± 2
GMRT	09PDA01	2005-11-26	53700.58	0.03	0.20	82	–	23 ± 4	84.5 ± 1.9
GMRT	09PDA01	2005-11-27	53701.59	0.07	0.20	164	–	35 ± 4	79.3 ± 1.2
GMRT	09PDA01	2005-11-29	53703.62	0.15	0.20	80	–	41 ± 4	72.8 ± 1.5
GMRT	09PDA01	2005-12-12	53716.70	0.64	0.21	60	–	56 ± 6	69.3 ± 1.6
GMRT	09PDA01	2005-12-13	53717.65	0.68	0.21	70	–	41 ± 2	58.5 ± 1.3
GMRT	09PDA01	2005-12-15	53719.61	0.75	0.21	80	–	38 ± 9	67.5 ± 1.5
GMRT	09PDA01	2005-12-16	53720.53	0.79	0.21	524	–	39.0 ± 1.9	61.2 ± 0.8
GMRT	09PDA01	2005-12-17	53721.56	0.82	0.21	130	–	33 ± 3	97.1 ± 1.1
GMRT	09PDA01	2005-12-18	53722.53	0.86	0.21	216	–	40 ± 4	92.1 ± 1.1
GMRT	09PDA01	2005-12-19	53723.53	0.90	0.21	80	–	43 ± 5	87.8 ± 1.7
GMRT	09PDA01	2005-12-29	53733.61	0.28	0.22	80	–	48 ± 11	64.8 ± 1.7
GMRT	09PDA01	2005-12-30	53734.49	0.31	0.22	80	–	–	58.8 ± 1.9
GMRT	09PDA01	2005-12-31	53735.41	0.35	0.22	56	–	53 ± 5	54 ± 3
GMRT	09PDA01	2006-01-08	53743.71	0.66	0.23	41	–	<69	26 ± 3
GMRT	09PDA01	2006-01-09	53744.36	0.68	0.23	144	–	<46	26.7 ± 0.7
GMRT	09PDA01	2006-01-10	53745.55	0.73	0.23	82	–	20 ± 4	33.9 ± 1.0
GMRT	09PDA01	2006-01-19	53754.67	0.07	0.23	82	–	–	93.6 ± 1.6
GMRT	09PDA01	2006-01-20	53755.49	0.10	0.23	70	–	36 ± 2	99.9 ± 1.6
GMRT	09PDA01	2006-01-21	53756.31	0.14	0.23	48	–	–	88.4 ± 1.1
GMRT	09PDA01	2006-02-05	53771.31	0.70	0.24	60	–	29 ± 5	64 ± 2
GMRT	09PDA01	2006-02-06	53772.27	0.74	0.24	82	–	<33	75.9 ± 1.4
GMRT	09PDA01	2006-02-07	53773.61	0.79	0.24	82	–	22 ± 5	90.3 ± 1.7
GMRT	13MPA01	2006-02-18	54514.28	0.74	0.69	662	52 ± 11[b]	–	–
GMRT	08DT051	2008-09-20	54729.90	0.88	0.82	492	–	140 ± 2	337 ± 3
LOFAR	L84298–L84317	2013-01-17	56309.83	0.51	0.76	200	32 ± 6[c]	–	–
LOFAR	L89566–L89589	2013-02-10	56333.71	0.41	0.78	116	<24[d]	–	–
LOFAR	L100374–L100397	2013-03-10	56361.67	0.47	0.80	116	<28[d]	–	–
LOFAR	L107793–L107816	2013-03-24	56375.58	0.99	0.80	116	77 ± 9[d]	–	–
LOFAR	L160534–L160557	2013-07-14	56487.42	0.21	0.87	116	31 ± 6[d]	–	–

Notes: [a]Pandey et al. (2007). [b]This observation was centred at 154 MHz with a bandwidth of 16 MHz. [c]This observation was centred at 142 MHz with a bandwidth of 2.3 MHz. [d]These observations were centred at 149 MHz with a bandwidth of 0.8 MHz.

conducted with a different setup: 20-min on-source runs centred at 142 MHz and divided into 12 subbands, with a total bandwidth of 2.4 MHz.

The LOFAR data were calibrated using standard procedures within the LOFAR Imaging Tools (LOFIM, version 2.5.2, see Heald et al. 2010 and van Haarlem et al. 2013 for a detailed explanation). The data were initially flagged using standard settings of the AOFLAGGER (Offringa, van de Gronde & Roerdink 2012), and averaged in time and frequency with the LOFAR New Default Pre-Processing Pipeline (NDPPP) with an integration time of 10 s and 4 channels per subband. In general, very bright sources did not need to be demixed from the target data sets, as they did not contribute significantly to the visibilities.[5]

The calibration was performed on each subband individually with the BlackBoard Selfcal (BBS) package using standard settings, and the solutions were transferred to the target field. We used an initial sky model for the field of LS I +61 303 based on the VLA Low-Frequency Sky Survey (Cohen et al. 2007). A manual flagging was performed using the `casaviewer` and `casaplotms` tasks from CASA[6] and the imaging process was conducted with a development version of AWIMAGER (Tasse et al. 2013). The resulting model was used in a later phase self-calibration, and we imaged the data again. The last two tasks were performed recursively between 2 and 5 times until the solutions converged. Due to the bright extended emission that is detected in the field of LS I +61 303 (located in the region of the Heart Nebula, see Fig. 2), we only kept baselines larger than 0.2 kλ (or 400 m) in subsequent analyses. Although the maximum baseline in the recorded data was ∼85 kλ (or 170 km), the baselines $\gtrsim$8 kλ (17 km) were removed during the data reduction (either during the manual flagging or during the self-calibration process). We used a Briggs robust weighting of zero again, because it produced the lowest noise level in the final images, and a pixel size of 10 arcsec.

We used the `imstat` and `imfit` tasks from CASA (both equivalent to the `tvstat` and `jmfit` tasks from AIPS used for the GMRT data) to measure the LS I +61 303 flux densities and the rms of the images. To guarantee the reliability of the measured flux densities

[5] The demixing process consists of removing from the target field visibilities the interference produced by the strongest off-axis sources in the sky, the so-called A-team: Cyg A, Cas A, Tau A, Vir A, Her A and Hyd A.

[6] The Common Astronomy Software Applications, CASA, is developed by the National Radio Astronomy Observatory (NRAO). http://casa.nrao.edu.

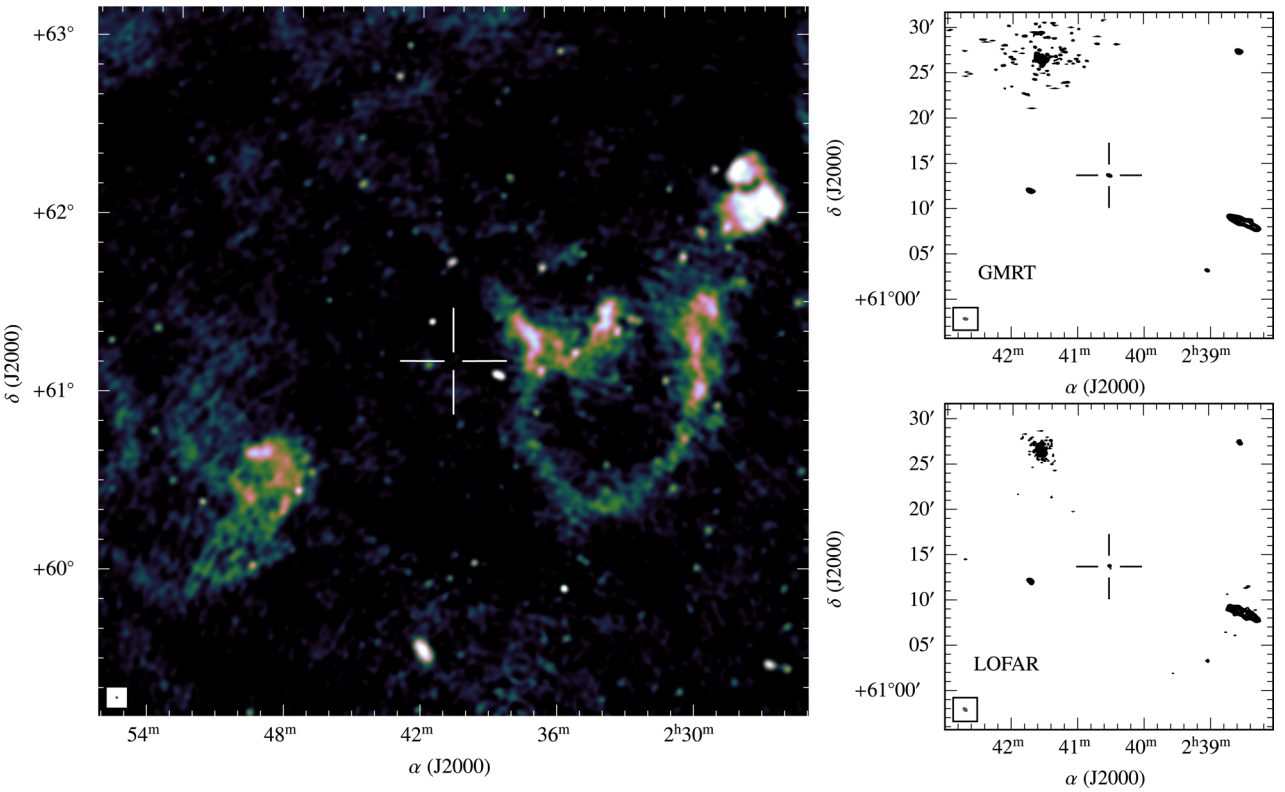

Figure 2. Left: field of LS I +61 303 observed with LOFAR at 149 MHz on 2013 July 14 without performing any cut in the *uv*-distance. The synthesized beam, shown in the lower-left corner, is 23 × 15 arcsec^2 with a PA of 64°, and the rms is 8 mJy beam^{-1} around the target source position. The positions of the sources present displacements of about half a synthesized beam, on average, with respect to the previously recorded ones (see text). The location of LS I +61 303 is marked with the white cross. The source is masked by extended emission from the Heart Nebula in this image. Right: zoom around the position of LS I +61 303 in the 154-MHz GMRT observation (top) and in the 2013 March 24 149-MHz LOFAR observation applying the final cut at baselines below 0.2 kλ (bottom). The source is clearly detected in both images. The synthesized beams, shown on the bottom-left corner, are 27 × 12 arcsec^2 with a PA of 80°, and 27 × 15 arcsec^2 with a PA = 49°, and the rms values are 11 and 6 mJy beam^{-1}, respectively. Contours start at 5σ noise level and increase by factors of $2^{1/2}$. In the GMRT image (top), we have applied a shift of 25 arcsec to recover the proper astrometric positions. No shift is required in the LOFAR image (bottom).

in the LOFAR images, we monitored the same four background sources chosen in the GMRT images. The lack of a similar trend in all sources, exhibiting consistent values with the ones inferred from the GMRT images, allows us again to be confident about the absence of flux calibration issues above the noise level in the LOFAR data.

We note that given the large field of view of these low-frequency images (either from the GMRT data or from the LOFAR ones), we detect differences in the ionospheric refractive effects for different regions across the field of view. These effects, in combination with the self-calibration cycles performed during the reduction process, produce slight displacements of the sources from their original positions. In general, it is common to end up with differences of up to the order of the synthesized beam size, although with differences in moduli and direction for different regions of the field.

2.3 Complementary 15-GHz observations

Two complementary observing campaigns that were conducted at the same epochs as the GMRT monitoring and the LOFAR observations have also been included in this work.

The RT (Pooley & Fender 1997) has observed LS I +61 303 at 15 GHz over many years, with contemporaneous observations during the epoch at which the 2005–2006 GMRT monitoring was performed. The observations are centred at 15.2 GHz, recording Stokes $I + Q$ and a bandwidth of 350 MHz. The four mobile and one fixed antennas were arranged in a compact configuration, with a maximum baseline of 100 m.

The observing technique is similar to that described in Pooley & Fender (1997). Given that we used baselines up to 100 m, we obtained a resolution in mapping mode of about 30 arcsec. The observations included regular visits to a phase calibrator (we used J0228+6721) to allow corrections for slow drifts of instrumental phase; the flux-density scale was established by nearby observations of 3C 48, 3C 147 or 3C 286.

Observations of LS I +61 303 were also conducted with the OVRO 40-m dish covering the epoch of the 2013 LOFAR observations. These data are part of a long-term monitoring that has been presented in Massi, Jaron & Hovatta (2015). The data were reduced by these authors following the procedures described in Richards et al. (2011).

3 RESULTS

LS I +61 303 appears as a point-like source in all the images. The resulting synthesized beams for the GMRT data range from 30 × 14 arcsec^2 to 15 × 5.4 arcsec^2, from 154 to 610 MHz, respectively. The synthesized beam for the LOFAR data is about 20 × 15 arcsec^2. The left-hand panel of Fig. 2 shows the field of LS I +61 303 obtained from the LOFAR observation conducted on 2013 July

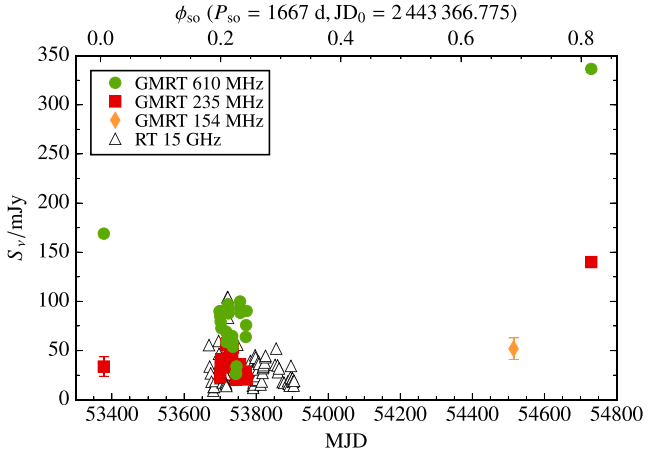

Figure 3. Flux density values of LS I +61 303 as a function of the MJD obtained from all the analysed GMRT data (2005–2008). We show the superorbital phase, ϕ_{so}, on the top x-axis. The green circles represent the 610-MHz data, the red squares the 235-MHz data, and the orange diamond the 154-MHz ones. The grey triangles represent the daily averages of the RT data at 15 GHz. Error bars represent 1σ uncertainties (smaller than the data points when they are not visible). We note that the source exhibits larger flux densities during the isolated GMRT observations (at superorbital phases of $\phi_{so} \approx 0.80$–0.95) than during the GMRT monitoring ($\phi_{so} \approx 0.2$).

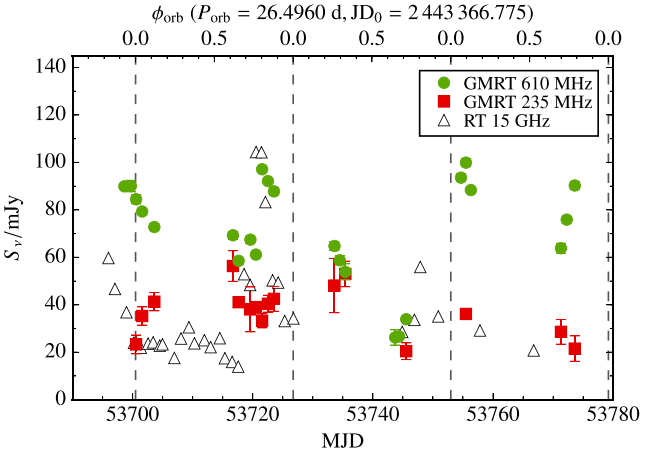

Figure 4. Same as Fig. 3 but zooming in on the GMRT monitoring observations. In this case we show the orbital phase, ϕ_{orb}, on the top x-axis. The vertical dashed lines show the epochs at which $\phi_{orb} = 0$. We observe the presence of enhanced emission at 610 MHz coincident with the outbursts at 15 GHz but with a slower decay (see MJD 52695–52705, 53720–53725). In contrast, at 235 MHz we observe a smaller degree of variability, with no clear orbital trends. The arrows represent the 3σ upper limits.

14 without applying any *uv*-cut during the imaging process. The zoomed images (Fig. 2, right) show the source as seen from the 154-MHz GMRT observation and from one of the LOFAR runs that we have analysed in this work. The flux density values of all the GMRT and LOFAR observations are shown in Table 1. In this section, we discuss the light curves obtained from the 235/610-MHz GMRT monitoring and from the ≈150-MHz LOFAR observations, including the 154-MHz GMRT data.

3.1 Light curves at 235 and 610 MHz

The dual 235/610-MHz mode in the GMRT observations allows us to observe the state of LS I+61 303 and its evolution simultaneously at these two frequencies. Fig. 3 shows the flux densities of all the analysed GMRT observations (the GMRT monitoring at 235 and 610 MHz and the three isolated GMRT observations) as a function of the Modified Julian Date (MJD, bottom axis) and the superorbital phase (ϕ_{so}, top axis). We observe that the flux densities obtained in the GMRT monitoring at 610 MHz (conducted at $\phi_{so} \approx 0.2$, around the minimum activity of LS I +61 303 at GHz frequencies) are significantly lower than the ones obtained in the other two observations (conducted at $\phi_{so} \approx 0.8$–0.0, during the maximum activity). We also observe this effect at 235 MHz with respect to the observation at $\phi_{so} \approx 0.8$ (but not at $\phi_{so} \approx 0.0$). This indicates the existence of the superorbital variability at frequencies below 1 GHz.

Fig. 4 focuses on the GMRT monitoring, showing the 610 and 235-MHz light curve of LS I +61 303 along three consecutive orbital cycles. The 610-MHz data exhibit variability with maxima roughly coincident with the outbursts observed in the 15-GHz RT data (e.g. see MJD ∼ 53720). However, at 610 MHz we observe that the decay of the emission is slower (e.g. compare the decays in MJD 53695–53705, 53720–53725). The average flux density during the whole monitoring is 70 mJy, with a standard deviation of 20 mJy and a significant variability. For these variability analyses (and in the rest of this work), we have taken the most conservative choice to consider the 3σ upper limits as the possible flux density value

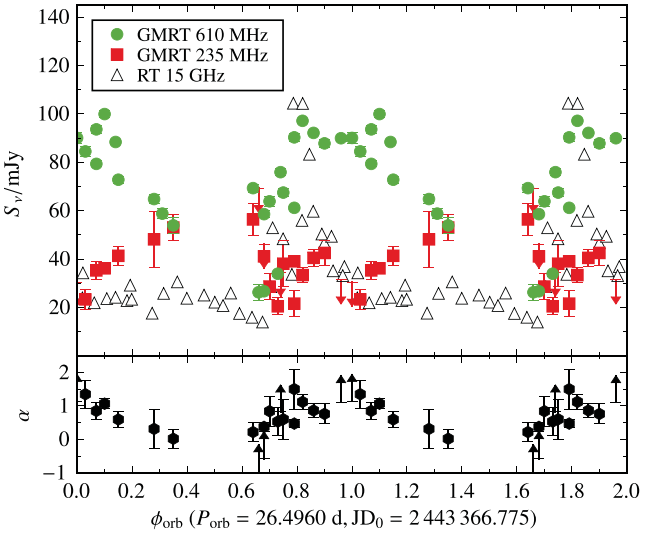

Figure 5. Top: folded light curve with the orbital period of the data shown in Fig. 4. The 610 MHz data show a quasi-sinusoidal modulation with enhanced emission at $\phi_{orb} \approx 0.8$–1.1, whereas the 15-GHz outbursts take place at $\phi_{orb} \approx 0.8$ with a fast decay. The 235 MHz light curve is almost anticorrelated with the one observed at 610 MHz. Bottom: spectral index α derived from the GMRT data presented above. Open hexagons represent the spectral index from the isolated GMRT data (not shown on top). Error bars represent 1σ uncertainties and the arrows represent the 3σ upper/lower limits.

of the source, assuming $S_\nu \approx 3\sigma \pm \sigma$. At 235 MHz we observe a smaller degree of variability, with no clear correlation with the previous one. In this case, we infer an average flux density of 37 ± 8 mJy and a variability at a 6σ confidence level.

Folding these data with the orbital phase (Fig. 5, top), we clearly see that the radio emission is orbitally modulated. At 610 MHz, we observe that the enhanced emission takes place in the range of $\phi_{orb} \sim 0.8$–1.1, whereas at 15 GHz the maximum occurs at $\phi_{orb} \approx 0.8$ and shows a faster decay. At 235 MHz, we observe that the flux density increases between $\phi_{orb} \sim 0.0$ and 0.4. This phase range is

followed by an interval without data between phases 0.4 and 0.6, after which we observe the largest flux density value followed by a fast decrease in the flux density. The increase and decrease of the flux density are traced by 4–5 data points in each case. Therefore, we observe that the maximum emission probably occurs in the range between $\phi_{\rm orb} \approx 0.3$ and ≈ 0.7, which is the location of the minimum at 610 MHz. In fact, the 235 MHz and the 610 MHz light curves are almost anticorrelated. Fig. 5 (bottom) shows the spectral index α (determined from the 235 and 610 MHz data) as a function of the orbital phase. The spectral index is also orbitally modulated, following essentially the 610-MHz flux density emission. From the isolated GMRT observations we obtain a spectral index coincident with the modulation observed from the GMRT monitoring, despite the much larger flux density values (see open hexagons in Fig. 5, bottom). We note that Fig. 5 shows data from different orbital cycles that have been poorly sampled. In addition, we remark that the outbursts seen at GHz frequencies exhibit changes from cycle to cycle. Therefore, we note that the profile seen in the folded light curve is different from the one we would obtain in a single orbital cycle.

3.2 Light curve at ≈ 150 MHz

Several data sets at a frequency around 150 MHz have been analysed: one GMRT observation at 154 MHz, one LOFAR observation at 142 MHz and four LOFAR observations at 149 MHz. In the following, we will refer to all these observations generically as 150-MHz observations. We note that the differences between these frequencies would not imply any significant change in the flux density values of LS I +61 303 for reasonable spectral indices.

The 150-MHz GMRT data (obtained at a superorbital phase of $\phi_{\rm so} \approx 0.69$) reveal for the first time a detection of LS I +61 303 at this frequency,[7] being a point-like source with a flux density of 52 ± 11 mJy.

The 150-MHz LOFAR observations taken within the RSM in 2013 ($\phi_{\rm so} \approx 0.76$–$0.87$) allow us to obtain a light curve of the source on week time-scales (spread along 7 orbital cycles). These results are shown in Fig. 6. With these data we clearly detect variability and a strong increase in the flux density of at least a factor of 3 in only 14 d between MJD 56361 and 56375 (approximately half of the orbital period). Folding these data with the orbital period, and adding the GMRT data at approximately the same frequency, we obtain the light curve shown in Fig. 7. We note that all these observations were conducted at similar superorbital phases. We observe a kind of baseline state with flux densities around 30 mJy on top of which there is a stronger emission between $\phi_{\rm orb} \approx 0.7$–$1.0$ (given the reduced coverage of the orbit, we certainly cannot constrain this range and it could actually be wider). Despite the poor sampling, the onset of the outburst at 150 MHz could take place at the same orbital phase as in the contemporaneous 15-GHz OVRO data, although the maximum of the outburst appears to be delayed at 150 MHz. The average flux density for these 150-MHz observations is 35 ± 16 mJy (considering the upper limits as the possible flux density value of the source: $S_\nu \approx 3\sigma \pm \sigma$).

[7] We note that LS I +61 303 was inadvertently detected at ≈150 MHz in a study of the Galactic emission made by Bernardi et al. (2009) with the Westerbork Synthesis Radio Telescope. The source is marginally detected in the figs 2 and 3 of Bernardi et al. (2009), close to the edge of the primary beam. At these positions the flux density measurements are much less reliable, and thus we will not discuss these data here. We also note that the positions of the sources in the mentioned figures present a general displacement of about 5 arcmin to the east direction with respect to the real positions.

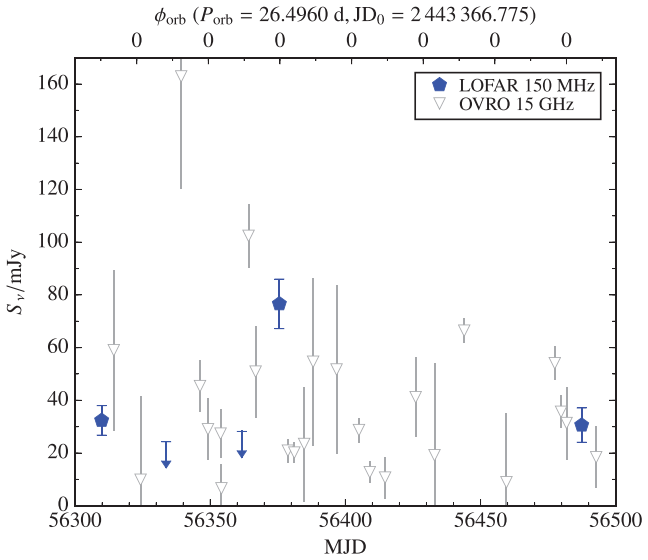

Figure 6. Flux density values of LS I +61 303 as a function of the MJD obtained from the 150-MHz LOFAR observations (conducted at $\phi_{\rm so} \approx 0.8$). We show the orbital phase, with labels every $\phi_{\rm orb} = 0$, on the top x-axis. We detect variability and a strong increase in the flux density of LS I +61 303 of at least a factor of 3 in only 14 d (between MJD 56361 and 56375). The open triangles represent the contemporaneous OVRO data at 15 GHz.

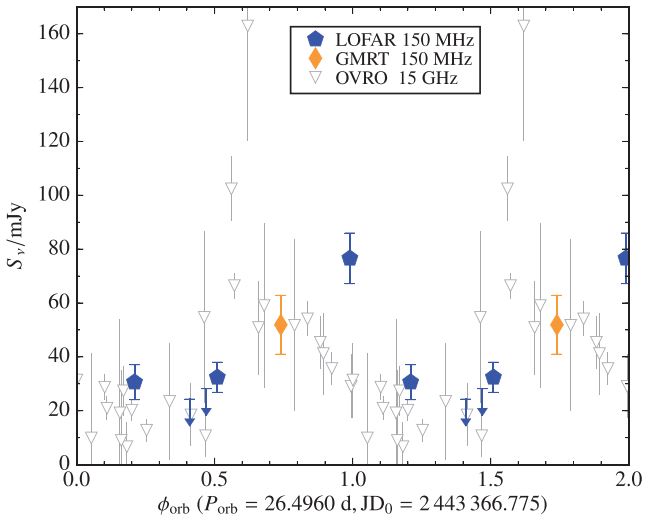

Figure 7. Folded light curve with the orbital period from the data shown in Fig. 6 plus the 150-MHz GMRT observation (orange diamonds). The flux density is orbitally modulated, exhibiting an enhanced emission at $\phi_{\rm orb} \approx 0.7$–$1.0$. Due to the poor sampling, we cannot determine the delay of the peak emission between 150 MHz and 15 GHz, although a delay seems to be observed between these frequencies.

4 DISCUSSION

We have presented here data of the gamma-ray binary LS I +61 303 at low radio frequencies, from 150 to 610 MHz. This is the first time that a gamma-ray binary is detected at 150 MHz, although previous searches have been performed in other sources (see Marcote et al. 2015, for the case of LS 5039). A multifrequency monitoring conducted with the GMRT in 2005–2006 (at a superorbital phase

of $\phi_{so} \approx 0.2$) shows significant variability at 610 MHz with the maximum emission at orbital phases of $\phi_{orb} \approx 0.8$–1.1. This variability is roughly coincident with the outbursts observed at 15 GHz, but with a significantly wider shape, a delay of about 0.2 orbital phases, and a slower decay. However, at 235 MHz we show that the maximum emission of the source occurs in the range between $\phi_{orb} \approx 0.3$ and $\approx$0.7. The light curve is thus almost anticorrelated with respect to the 610-MHz one. The LOFAR observations were conducted, in contrast, at a superorbital phase of $\phi_{so} \approx 0.8$. In this case, we observe a behaviour similar to the one observed at 610 MHz: a large variability with the maximum emission taking place at orbital phases between 0.7 and 1.0.

In this section, we discuss the observed behaviour at 150, 235 and 610 MHz and its relationship with the superorbital modulation. It must be noted that the compact VLBI radio emission detected at GHz frequencies represents $\gtrsim$90 per cent of the total flux density of LS I +61 303, leaving small room for extended radio emission (Paredes et al. 1998). For that reason, and also because of the limited number of frequencies with available light curves (and the use of data from different orbital cycles), we assume a one-zone model with an homogeneous emitting region. We consider here the two most probable absorption mechanisms: FFA and SSA (there are not enough data to consider the Razin effect such as in Marcote et al. 2015). We infer the physical changes required in the system to explain the observed delay between the orbital phases at which the maximum emission takes place at different frequencies.

From Fig. 3, we observe that the superorbital phase still has an important role at these low frequencies, as we detect a much larger flux density at high ϕ_{so} than at low ones. Given that we only have two isolated observations at high superorbital phases, we cannot determine what was the state of the source during these observations (maximum of the orbital variability, minimum or in between). Therefore, we cannot accurately estimate the increase of the emission as a function of the superorbital phase.

A correlation between changes in the thermal emission of the circumstellar disc, observed from optical photometry and Hα observations, and the superorbital modulation of the non-thermal emission has been reported (Paredes-Fortuny et al. 2015, and references therein). A larger amount of material in the disc (higher values of Hα equivalent width) is observed at superorbital phases coincident with the maximum emission at GHz frequencies ($\phi_{so} \sim 0.8$–0.0). This larger amount of material in the disc might imply more target material for a shock with the putative pulsar wind. This could potentially lead to a more efficient particle acceleration and stronger emission, but also to a larger absorption at low radio frequencies. The presence of stronger radio emission and a clear variability at 150 MHz at these superorbital phases indicates that the emission increase, probably produced as a result of the more efficient particle acceleration, seems to dominate over the decrease due to enhanced absorption at these low radio frequencies.

The positive spectral indices obtained from the GMRT monitoring (Fig. 5, bottom) confirm the suggestion of a turnover between 0.3 and 1.4 GHz made by Strickman et al. (1998), and we constrain it to be in the 0.6–1.4 GHz range. Assuming that the spectrum at low frequencies is dominated by FFA, we can estimate the radius of the emitting region with the condition that the free–free opacity is

$$\tau_{ff} \approx 30 \dot{M}_{-7}^{2} \nu_{GHz,max}^{-2} \ell_{au}^{-3} v_{W,8.3}^{-2} T_{W,4}^{-3/2} = 1, \quad (1)$$

where $\dot{M}_{-7}$ is the mass-loss rate of the companion star in units of $10^{-7}\,M_{\odot}\,yr^{-1}$, $\nu_{GHz,\,max}$ is the frequency at which the maximum emission takes place (or turnover frequency), in GHz units, ℓ_{au} is the radius in the spherically symmetric case, measured in au, $v_{W,\,8.3}$ is the velocity of the stellar wind, in units of 2×10^{8} cm s^{-1} and $T_{W,\,4}$ is the wind temperature, in units of 10^{4} K (Rybicki & Lightman 1979). Assuming a luminosity of $L \sim 4.65\,L_{\odot}$, typical from B0 V stars, we derive a mass-loss rate of $\dot{M}_{-7} \sim 0.5$ (Howarth & Prinja 1989), for which we will assume reasonable values in the range of $\dot{M}_{-7} \sim 0.2$–1. Considering the effective temperature of $T_{eff} \sim 28\,000$ K, also expected for this type of star (Cox 2000), we deduce a wind velocity of $1\,500 \pm 500$ km s^{-1} (or $v_{W,\,8.3} \sim 0.75$; Kudritzki & Puls 2000). We also expect a wind temperature of $\sim$10 000 K at a distance of the order of the apastron (Krtička & Kubát 2001), and a turnover frequency $\nu_{GHz,\,max} \sim 1$ (as mentioned before). With these values we estimate a radius for the spherically emitting region of $2.4^{+1.7}_{-1.1}$ au.

We can compare this result with the displacements of the peak positions obtained with VLBA observations along one orbital cycle by Dhawan et al. (2006). From their fig. 4 we observe displacements as large as $\sim$2.5 and $\sim$2 mas ($\sim$5 and $\sim$4 au) at 2.2 and 8.4 GHz, respectively, which in our spherically symmetric model imply radii of $\sim$2.5 and $\sim$2 au. Although we are using a spherical model, we note that the radius that we have derived is clearly compatible with these values, as expected considering that the emission has to be produced far away enough from the massive star to avoid being in the optically thick part of the spectrum due to FFA.

On the other hand, we can consider that the emitting region is expanding, and thus the turnover frequency evolves along the time. In this case, we consider that the transition from an optically thick to an optically-thin region would produce the delay between the different maxima observed at 235 and 610 MHz, as previously reported for other binary systems (Ishwara-Chandra, Yadav & Pramesh Rao 2002). From equation (1), we can determine the radius of the emitting region when the turnover is located at a frequency ν:

$$\ell_{\nu} = 30^{1/3}\, \dot{M}_{-7}^{2/3}\, v_{W,8.3}^{-2/3}\, T_{W,4}^{-1/2}\, \nu^{-2/3}. \quad (2)$$

With this relation we can infer the velocity of the expanding emitting region, or expansion velocity, assuming it to be constant for simplicity:

$$v = \frac{\Delta \ell}{\Delta t} = \frac{\ell_{\nu_2} - \ell_{\nu_1}}{\Delta \phi\, P_{orb}}, \quad (3)$$

where $\Delta\phi$ is the shift in orbital phase for the maximum at a frequency ν_2 and ν_1, and P_{orb} is the orbital period. We can consider for simplicity the case that $\dot{M}_{-7}$, $v_{W,\,8.3}$ and $T_{W,\,4}$ remain constant during this expansion. Figs 4 and 5 show that the peak of the emission at 610 MHz is located somewhere between $\phi_{orb} \sim 0.8$ and 1.1. In parallel, we observe that the flux density at 235 MHz remains increasing at $\phi_{orb} \sim 0.4$, and in the range of 0.6–0.7 the flux density is already decreasing. Therefore, the maximum emission probably takes place in the range of 0.3–0.7. These values imply that the maximum emission exhibits a shift of $\approx$0.2–0.9 in orbital phase between the two frequencies. Although the uncertainty in this shift is large, we can assume a shift of $\sim$0.5 to provide a rough estimation of the expansion velocity for the radio emitting region. Assuming this value and with all the previously mentioned data, we infer that the emitting region should expand by a factor of 2.0 $\pm$ 0.5 during this delay of $\approx$0.5 in orbital phase ($\approx$13 d) from 610 to 235 MHz, implying a constant expansion velocity of $v_{FFA} = 350 \pm 220$ km s^{-1}. If we also consider the shifts in orbital phase with respect to the maximum at 15 GHz, we can deduce,

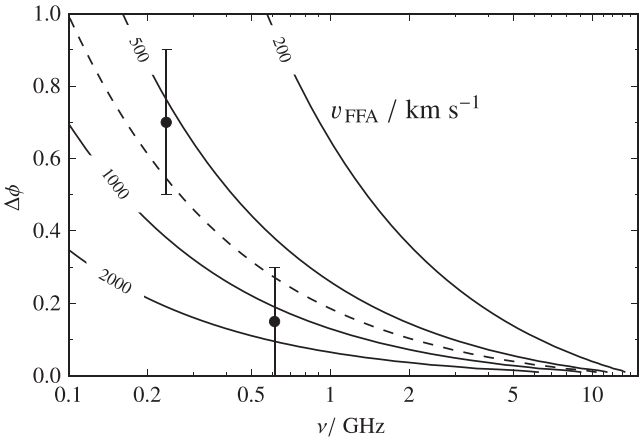

Figure 8. Shift in orbital phase ($\Delta\phi$) expected for the maxima in the flux density emission between a frequency ν and 15 GHz for different velocities of expansion of the radio emitting region ($v_{\rm FFA}$) assuming that FFA is the dominant absorption process and following equation (4). The black circles represent the shifts at 235 and 610 MHz with respect to 15 GHz in the folded light curve considered in the discussion. We fit the data with an expansion velocity of $\sim$700 km s^{-1} (dashed line).

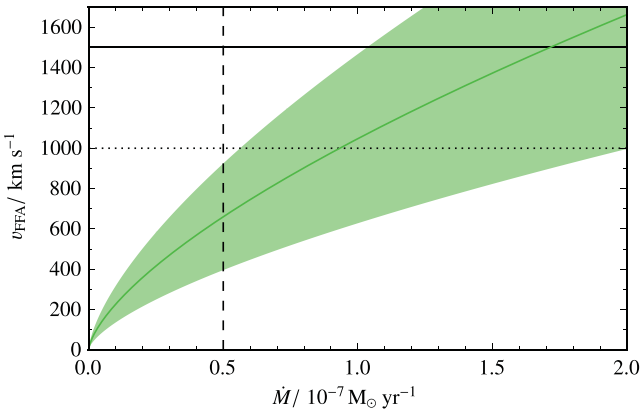

Figure 9. Velocities, $v_{\rm FFA}$, of the expanding emitting region as a function of the mass-loss rate, $\dot{M}$, derived from the considered delay between the maxima at 235 and 610 MHz with respect to 15 GHz, assuming a free–free absorbed region. The green curve represents the mean derived velocity and the light green shaded region represents the possible velocity values by considering the uncertainties in the orbital phase shifts between different frequencies, and in the stellar wind velocity. The vertical dashed line denotes the derived mass-loss rate. The horizontal lines represent the mean and lower value of the stellar wind velocity (solid and dotted line, respectively).

from equations (2) and (3), the expected delay in orbital phase as a function of the velocity, $v_{\rm FFA}$, and the frequency, ν:

$$\Delta\phi_{\rm FFA} = \frac{30^{1/3}\,\dot{M}_{-7}^{2/3}\,v_{\rm W,8.3}^{-2/3}\,T_{\rm W,4}^{-1/2}}{v_{\rm FFA}\,P_{\rm orb}}\left(\nu_{\rm GHz}^{-2/3} - 15^{-2/3}\right). \quad (4)$$

Fig. 8 shows the velocity curves derived from this equation, where a fit to the considered shifts at 235 and 610 MHz with respect to 15 GHz produces a constant velocity of $v_{\rm FFA} = 660 \pm 280$ km s^{-1}. This velocity is a factor of $\sim$2 smaller than the one of the stellar wind. However, the derived velocity depends strongly on the assumed mass-loss rate, which is unconstrained from the observational point of view. Fig. 9 shows the derived expansion velocity of the emitting region for different values of the mass-loss rate (in Fig. 8 we assumed $\dot{M}_{-7} = 0.5$). We note that for mass-loss rates of $\dot{M}_{-7} \approx 1$ (which is still possible) the derived velocities overlap with the range of possible stellar wind velocities. In any case, these velocities are much lower than the relativistic velocity of the putative pulsar wind (see discussion in Bogovalov et al. 2012). Dhawan et al. (2006) estimated the outflow velocity along the orbit at 2.2 and 8.4 GHz, obtaining maximum values of $\sim$7500 km s^{-1} near periastron and $\sim$1000 km s^{-1} near apastron. Therefore, the expansion velocities derived here are also close to the one derived by these authors near apastron.

If instead of FFA we consider SSA as the dominant absorption process at low frequencies, we can estimate the properties of the emitting region in the optically thick to optically thin transition. In this case, the SSA opacity is

$$\tau_{\rm SSA} = 3.354\times10^{-11}(3.54\times10^{18})^{p}\,K\,B^{(p+2)/2}\,b(p)\,\nu_{\rm GHz}^{-(p+4)/2}\,\ell_{\rm au} = 1, \quad (5)$$

where K is the normalization of the accelerated particles, B is the magnetic field, and $b(p)$ is a function that only depends on $p \equiv 1 - 2\alpha$ (Longair 2011). Assuming $p \sim 2$ (i.e. $\alpha \sim -0.5$ in the optically thin region, similar to the average spectral index observed in LS I +61 303 above $\sim$2 GHz) we would expect that the quantity $K B^2\,\ell$ decreases a factor of $\sim$18 during the delay of $\sim$0.5 in orbital phase between the maximum emission at 235 and 610 MHz. These three quantities (K, B, ℓ) are coupled in the equation above and thus we cannot estimate them separately. All of them would a priori change along the orbit, but since we assume an expanding region from the same population of accelerated particles, K should remain constant (provided that losses are not significant). Additionally, one can consider different dependences of B as a function of ℓ: $B \sim \ell^{-2}$ (as in a spherical expansion) or $B \sim \ell^{-1}$ (as in a conical or toroidal expansion, as it happens either in a relativistic jet from the microquasar scenario or in a cometary tail from the young non-accreting pulsar scenario). With these considerations we expect an expansion factor of $\sim$2.6 (if $B \sim \ell^{-2}$) or $\sim$18 (if $B \sim \ell^{-1}$). To derive the expansion velocity of the emitting region, we can assume the radius of $\ell = 2.4^{+1.7}_{-1.1}$ au that we have obtained at 1 GHz in the FFA case, which is also compatible with the results from Dhawan et al. (2006). With these assumptions, and the equations (3) and (5), we obtain the shifts in orbital phase between the maximum at a frequency ν and at 15 GHz:

$$\Delta\phi_{\rm SSA} = \frac{\nu_{\rm GHz}^{3} - 15^{3}}{v_{\rm SSA}\,P_{\rm orb}\,3.354\times10^{-11}(3.54\times10^{18})^{2}\,K\,B^{2}\,b(2)}. \quad (6)$$

Fig. 10 shows the derived velocity curves as a function of the frequency and the orbital phase shift for the SSA case. In the case of $B \sim \ell^{-2}$ we can fit the data with a constant velocity of $v_{\rm SSA} = 1000 \pm 200$ km s^{-1}, where the uncertainties result from the propagation of the uncertainties in ℓ at 1 GHz. The fitted velocity is also compatible with the one of the stellar wind. In the case of $B \sim \ell^{-1}$ the data are best fitted with a constant velocity of 17 000 $\pm$ 2000 km s^{-1}, which is significantly faster than the stellar wind one. In any case, both velocities in the SSA scenario are clearly slower than the relativistic velocity of the putative pulsar wind or the relativistic jet. We note that if energy losses were considered, the derived expansion velocities would be even lower than the ones discussed. A dependence of $B \sim \ell^{-1}$ would be more plausible given the *conical* geometry of the current scenarios, based either on a cometary tail or a jet. However, at least in the young non-accreting pulsar scenario, the emitting region at low frequencies could exhibit a more toroidal or spherical geometry after mixing with stellar wind, in which case a dependence closer to $B \sim \ell^{-2}$ would be expected.

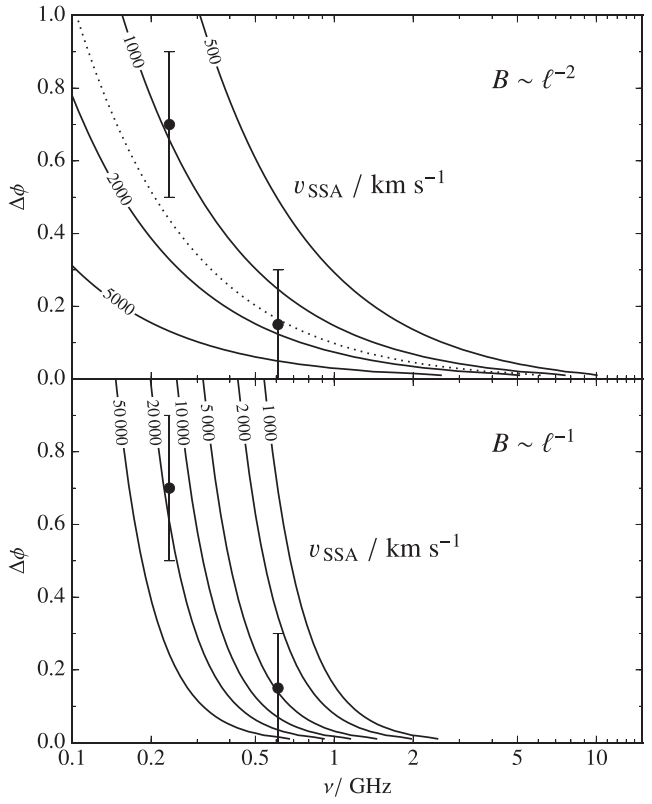

Figure 10. Same as Fig. 8 but assuming that SSA is the dominant absorption process and following equation (6). Two different dependences of B have been considered: $B \sim \ell^{-2}$ (top) or $B \sim \ell^{-1}$ (bottom). The dotted line on the top panel represents the mean value of the derived wind velocity. We note that with the dependence $B \sim \ell^{-2}$ (top) we can easily explain the data with an expansion velocity of $\sim$1000 km s^{-1}, while with the dependence $B \sim \ell^{-1}$ (bottom) a velocity of $\sim$17 000 km s^{-1} is required.

We show that either FFA or SSA (with different magnetic field dependences) can explain the delays of the low-frequency emission of LS I +61 303 with expansion velocities of $\sim$1000 or $\sim$17 000 km s^{-1}, depending on the considered model. On the one hand, a large expansion velocity of $\sim$17 000 km s^{-1} could be accommodated either in the young non-accreting pulsar scenario or in the microquasar one. In the first scenario, the obtained velocity would indicate that the stellar wind does not dominate the expansion of the emitting region. In the second one, this velocity could be an estimate of the lateral expansion velocity of the jet. On the other hand, low expansion velocities of $\sim$1000 km s^{-1} appear too low to represent the lateral expansion velocity of the jet, while they could be obtained in the young non-accreting pulsar scenario if the stellar wind dominates the expansion of the emitting region.

We can also compare the delays predicted by our models with the simultaneous data taken between 2.6 and 15 GHz in 2012, $\phi_{\rm so} \sim 0.6$ (Zimmermann, Fuhrmann & Massi 2015). These data show that the peak of the emission at these frequencies takes place at roughly the same orbital phases, setting a delay $\lesssim$0.05 within this frequency range. Although this delay is compatible with the three fitted models within uncertainties, we note that the FFA and SSA with $B \sim \ell^{-2}$ models predict delays closer to 0.1 orbital phases, while delays close to zero could only be reproduced by the SSA with $B \sim \ell^{-1}$ model. However, we stress that the superorbital phase of the 2012 observations is 0.6, different to the one of the GMRT monitoring (0.2), and thus the orbital variability as a function of the frequency could be different.

Extrapolating the obtained results to 150 MHz, we infer an orbital phase delay of about 0.9 (assuming FFA) or $\sim$1.0 (assuming SSA with $B \sim \ell^{-2}$). In the case of SSA with $B \sim \ell^{-1}$ we would expect a mixing between different outbursts. However, these results cannot be directly compared with the obtained light curves at 150 MHz. These data were taken at different superorbital phases ($\phi_{\rm so} \sim 0.9$ instead of $\sim$0.2), and we observe a larger flux density emission and a larger variability at these 150 MHz data than the ones expected from an extrapolation of the 235 and 610-MHz light curves. This implies, as mentioned before, that the superorbital phase still plays a significant role at low frequencies. In any case, the shift at 150 MHz with respect to the 15-GHz data is not well constrained and it could be between $\sim$0.0 and $\sim$0.5 orbital phases, with the possibility of observing a full cycle shift (and thus between 1.0 and 1.5). We note that these values are roughly compatible with the ones derived from the 235 and 610-MHz data assuming a one-cycle delay. However, we cannot discard the possibility of being observing a delay of only $\sim$0.0–0.5 orbital phases, as we would expect less absorption at these high superorbital phases, which would also explain why we see a large orbital variability.

5 CONCLUSIONS

We have detected for first time a gamma-ray binary, LS I +61 303, at a frequency as low as 150 MHz. This detection establishes the starting point to explore the behaviour of gamma-ray binaries in the low-frequency radio band, which will allow us to unveil the absorption processes that can occur in their radio spectra or light curves. Additionally, we have obtained light curves of LS I +61 303 at 150, 235 and 610 MHz, observing orbital and superorbital variability in all cases. In the folded light curve with the orbital period, we observe quasi-sinusoidal modulations with the maxima at different orbital phases as a function of the frequency. The observed delays between frequencies seem to be also modulated by superorbital the phase. The flux density values are also modulated by the superorbital phase, with the source displaying a stronger emission at $\phi_{\rm so} \sim 1$.

We have modelled the shifts between the maxima at different frequencies as due to the expansion of a one-zone spherically symmetric emitting region assuming either FFA or SSA with two different magnetic field dependences. The derived expansion velocities are clearly subrelativistic and in some cases close to the stellar wind one. Both the young non-accreting pulsar scenario and the microquasar scenario could accommodate the obtained highest velocities ($\sim$17 000 km s^{-1}), although the first scenario seems to be favoured in the case of low velocities ($\sim$1000 km s^{-1}), which are close to the stellar wind one.

The limited amount of data acquired up to now precludes detailed modelling to establish the origin of the variability at different frequencies and epochs. Further multi-epoch observations of LS I +61 303 with LOFAR are needed. These data would allow us to determine the light curve of LS I +61 303 folded in orbital phase and study its changes as a function of the superorbital phase. A good coverage of a single orbital cycle is mandatory to obtain a reliable profile of the variability of LS I +61 303 due to the significant differences observed between outbursts at different orbital phases. Future simultaneous multifrequency observations with the GMRT, LOFAR and the VLA at different superorbital phases would allow us to study the light curve of LS I +61 303 and its dependence with the frequency. These data could unveil the changes in the physical

parameters that characterize the emitting region and the absorption processes required to explain the superorbital modulation. Finally, the use of the International stations in LOFAR observations (longer baselines) would allow us to search for the extended emission at arcsec scales that is expected to arise at low frequencies.

ACKNOWLEDGEMENTS

We thank the anonymous reviewer for providing comments that helped to improve the original version of the manuscript. We thank the staff of the GMRT and LOFAR who made these observations possible. GMRT is run by the National Centre for Radio Astrophysics of the Tata Institute of Fundamental Research. LOFAR, the Low Frequency Array designed and constructed by ASTRON, has facilities in several countries, that are owned by various parties (each with their own funding sources), and that are collectively operated by the International LOFAR Telescope (ILT) foundation under a joint scientific policy. The RT is operated by the University of Cambridge and supported by STFC. This research has made use of data from the OVRO 40-m monitoring program which is supported in part by NASA grants NNX08AW31G and NNX11A043G, and NSF grants AST-0808050 and AST-1109911. We thank T. Hovatta for providing the OVRO 40-m dish data. BM, MR and JMP acknowledge support by the Spanish Ministerio de Economía y Competitividad (MINECO) under grants AYA2013-47447-C3-1-P, FPA2013-48381-C6-6-P, MDM-2014-0369 of ICCUB (Unidad de Excelencia 'María de Maeztu'), and the Catalan DEC grant 2014 SGR 86. BM acknowledges financial support from MINECO under grant BES-2011-049886. JMP acknowledges financial support from ICREA Academia. JWB acknowledges support from European Research Council Advanced Grant 267697 '4 Pi Sky: Extreme Astrophysics with Revolutionary Radio Telescopes'. RPB has received funding from the European Union Seventh Framework Programme under grant agreement PIIF-GA-2012-332393. SC acknowledges financial support from the UnivEarthS Labex program of Sorbonne Paris Cité (ANR-10-LABX-0023 and ANR-11-IDEX-0005-02). The financial assistance of the South African SKA Project (SKA SA) towards this research is hereby acknowledged. Opinions expressed and conclusions arrived at are those of the authors and are not necessarily to be attributed to the SKA SA.

REFERENCES

Abdo A. A. et al., 2009, ApJ, 706, L56
Acciari V. A. et al., 2008, ApJ, 679, 1427
Acciari V. A. et al., 2009, ApJ, 698, L94
Aharonian F. et al., 2005a, Science, 309, 746
Aharonian F. et al., 2005b, A&A, 442, 1
Albert J. et al., 2006, Science, 312, 1771
Albert J. et al., 2008, ApJ, 684, 1351
Albert J. et al., 2009, ApJ, 693, 303
Ananthakrishnan S., 1995, JA&AS, 16, 427
Anderhub H. et al., 2009, ApJ, 706, L27
Aragona C., McSwain M. V., Grundstrom E. D., Marsh A. N., Roettenbacher R. M., Hessler K. M., Boyajian T. S., Ray P. S., 2009, ApJ, 698, 514
Bernardi G. et al., 2009, A&A, 500, 965
Bignami G. F., Caraveo P. A., Lamb R. C., Markert T. H., Paul J. A., 1981, ApJ, 247, L85
Bogovalov S. V., Khangulyan D., Koldoba A. V., Ustyugova G. V., Aharonian F. A., 2012, MNRAS, 419, 3426
Bosch-Ramon V., 2009, A&A, 493, 829
Briggs D. S., 1995, BAAS, 27, 1444
Cañellas A., Joshi B. C., Paredes J. M., Ishwara-Chandra C. H., Moldón J., Zabalza V., Martí J., Ribó M., 2012, A&A, 543, A122
Casares J., Ribas I., Paredes J. M., Martí J., Allende Prieto C., 2005, MNRAS, 360, 1105
Cohen A. S., Lane W. M., Cotton W. D., Kassim N. E., Lazio T. J. W., Perley R. A., Condon J. J., Erickson W. C., 2007, ApJ, 134, 1245
Cotton W. D., 2008, PASP, 120, 439
Cox A. N., 2000, Allen's Astrophysical Quantities. Am. Inst. Phys., New York
Dhawan V., Mioduszewski A., Rupen M., 2006, in Belloni T., ed., Proc. VI Microquasar Workshop: Microquasars and Beyond, Como, Italy, p. 52
Dubus G., 2006, A&A, 456, 801
Dubus G., 2013, A&AR, 21, 64
Durant M., Kargaltsev O., Pavlov G. G., Chang C., Garmire G. P., 2011, ApJ, 735, 58
Fender R., Wijers R., Stappers B., LOFAR Transients Key Science Project 2007, in Tzisumis L., Fender, eds, Proc. Bursts, Pulses and Flickering: Wide-field Monitoring of the Dynamic Radio Sky. Kerastari, Tripolis, Greece, p. 30
Fermi LAT Collaboration et al., 2012, Science, 335, 189
Frail D. A., Hjellming R. M., 1991, ApJ, 101, 2126
Gregory P. C., 2002, ApJ, 575, 427
Gregory P. C., Xu H.-J., Backhouse C. J., Reid A., 1989, ApJ, 339, 1054
Heald G. et al., 2010, in Proc. ISKAF2010 Science Meeting, Assen, the Netherlands, p. 57
Hermsen W. et al., 1977, Nature, 269, 494
Hinton J. A. et al., 2009, ApJ, 690, L101
Howarth I. D., Prinja R. K., 1989, ApJS, 69, 527
Intema H. T., van der Tol S., Cotton W. D., Cohen A. S., van Bemmel I. M., Röttgering H. J. A., 2009, A&A, 501, 1185
Ishwara-Chandra C. H., Yadav J. S., Pramesh Rao A., 2002, A&A, 388, L33
Kettenis M., van Langevelde H. J., Reynolds C., Cotton B., 2006, in Gabriel C., Arviset C., Ponz D., Enrique S., eds, ASP Conf. Ser. Vol. 351, Astronomical Data Analysis Software and Systems XV. Astron. Soc. Pac., San Francisco, p. 497
Kniffen D. A. et al., 1997, ApJ, 486, 126
Krtička J., Kubát J., 2001, A&A, 377, 175
Kudritzki R.-P., Puls J., 2000, ARA&A, 38, 613
Longair M. S., 2011, High Energy Astrophysics, 3rd edn. Cambridge Univ. Press, Cambridge
McSwain M. V., Ray P. S., Ransom S. M., Roberts M. S. E., Dougherty S. M., Pooley G. G., 2011, ApJ, 738, 105
Marcote B., Ribó M., Paredes J. M., Swinbank J., Broderick J., Fender R., Markoff S., Wijers R., 2012, in Aharonian F. A., Hofmann W., Rieger F. M., eds, AIP Conf. Proc. Vol. 1505, High Energy Gamma-Ray Astronomy: 5th International Meeting on High Energy Gamma-Ray Astronomy. Am. Inst. Phys., New York, p. 374
Marcote B., Ribó M., Paredes J. M., Ishwara-Chandra C. H., 2015, MNRAS, 451, 4578
Massi M., Torricelli-Ciamponi G., 2014, A&A, 564, A23
Massi M., Ribó M., Paredes J. M., Peracaula M., Estalella R., 2001, A&A, 376, 217
Massi M., Ribó M., Paredes J. M., Garrington S. T., Peracaula M., Martí J., 2004, A&A, 414, L1
Massi M., Ros E., Zimmermann L., 2012, A&A, 540, A142
Massi M., Jaron F., Hovatta T., 2015, A&A, 575, L9
Mirabel I. F., 2006, Science, 312, 1759
Moldón J., 2012, PhD thesis, Univ. Barcelona
Offringa A. R., van de Gronde J. J., Roerdink J. B. T. M., 2012, A&A, 539, A95
Pandey M., Rao A. P., Ishwara-Chandra C. H., Durouchoux P., Manchanda R. K., 2007, A&A, 463, 567
Paredes J. M., 1987, PhD thesis, Univ. Barcelona
Paredes J. M., Estalella R., Rius A., 1990, A&A, 232, 377
Paredes J. M., Martí J., Peracaula M., Ribó M., 1997, A&A, 320, L25
Paredes J. M., Massi M., Estalella R., Peracaula M., 1998, A&A, 335, 539
Paredes-Fortuny X., Ribó M., Bosch-Ramon V., Casares J., Fors O., Núñez J., 2015, A&A, 575, L6
Pooley G. G., Fender R. P., 1997, MNRAS, 292, 925

Ray P. S., Foster R. S., Waltman E. B., Tavani M., Ghigo F. D., 1997, ApJ, 491, 381
Richards J. L. et al., 2011, ApJS, 194, 29
Rybicki G. B., Lightman A. P., 1979, Radiative Processes in Astrophysics. Wiley-Interscience, New York
Skilton J. L. et al., 2009, MNRAS, 399, 317
Strickman M. S., Tavani M., Coe M. J., Steele I. A., Fabregat J., Marti J., Paredes J. M., Ray P. S., 1998, ApJ, 497, 419
Tasse C., van der Tol S., van Zwieten J., van Diepen G., Bhatnagar S., 2013, A&A, 553, A105
Thompson A. R., 1999, in Taylor G. B., Carilli C. L., Perley R. A., eds, ASP Conf. Ser. Vol. 180, Synthesis Imaging in Radio Astronomy II. Astron. Soc. Pac., San Francisco, p. 11
van Haarlem M. P. et al., 2013, A&A, 556, A2
Zamanov R., Stoyanov K., Martí J., Tomov N. A., Belcheva G., Luque-Escamilla P. L., Latev G., 2013, A&A, 559, A87
Zimmermann L., Fuhrmann L., Massi M., 2015, A&A, 580, L2

[1]*Departament d'Astronomia i Meteorologia, Institut de Ciències del Cosmos, Universitat de Barcelona, IEEC-UB, Martí i Franquès 1, E-08028 Barcelona, Spain*
[2]*National Centre for Radio Astrophysics, TIFR, Post Bag 3, Ganeshkhind, 411007 Pune, India*
[3]*Department of Astrophysical Sciences, Princeton University, Princeton, NJ 08544, USA*
[4]*Astrophysics, Department of Physics, University of Oxford, Keble Road, Oxford OX1 3RH, UK*
[5]*Department of Physics and Astronomy, University of Southampton, Highfield, Southampton SO17 1BJ, UK*
[6]*Anton Pannekoek Institute for Astronomy, University of Amsterdam, Science Park 904, NL-1098 XH Amsterdam, the Netherlands*
[7]*Mullard Radio Astronomy Observatory, Cavendish Laboratory, The University of Cambridge, J.J. Thomson Avenue, Cambridge CB3 0HE, UK*
[8]*CSIRO Astronomy and Space Science, PO Box 76, Epping, NSW 1710, Australia*
[9]*ARC Centre of Excellence for All-sky Astrophysics (CAASTRO), The University of Sydney, NSW 2006, Australia*
[10]*Jodrell Bank Centre for Astrophysics, School of Physics and Astronomy, The University of Manchester, Manchester M13 9PL, UK*
[11]*Laboratoire AIM (CEA/IRFU - CNRS/INSU - Université Paris Diderot), CEA DSM/IRFU/SAp, F-91191 Gif-sur-Yvette, France*
[12]*Station de Radioastronomie de Nançay, Observatoire de Paris, PSL Research University, CNRS, Univ. Orléans, OSUC, F-18330 Nançay, France*
[13]*Thüringer Landessternwarte, Sternwarte 5, D-07778 Tautenburg, Germany*
[14]*Department of Astrophysics/IMAPP, Radboud University Nijmegen, PO Box 9010, NL-6500 GL Nijmegen, the Netherlands*
[15]*ASTRON, the Netherlands Institute for Radio Astronomy, Postbus 2, NL-7990 AA Dwingeloo, the Netherlands*
[16]*LPC2E - Université d'Orléans / CNRS, F-45071 Orléans cedex 2, France*
[17]*NAOJ Chile Observatory, National Astronomical Observatory of Japan, 2-21-1 Osawa, Mitaka, Tokyo 181-8588, Japan*
[18]*Oxford Astrophysics, Denys Wilkinson Building, Keble Road, Oxford OX1 3RH, UK*
[19]*Department of Physics & Astronomy, University of the Western Cape, Private Bag X17, Bellville 7535, South Africa*
[20]*SKA South Africa, 3rd Floor, The Park, Park Road, Pinelands 7405, South Africa*
[21]*Department of Physics, The George Washington University, 725 21st Street NW, Washington, DC 20052, USA*
[22]*LESIA, Observatoire de Paris, CNRS, UPMC, Université Paris-Diderot, 5 place Jules Janssen, F-92195 Meudon, France*

This paper has been typeset from a TEX/LATEX file prepared by the author.